Transient Aseismic Slip Following 2017 Mw 7.3 Sarpol-e Zahab, Iran, Earthquake: Possible Evidence for Fault Frictional Heterogeneity and Thin-skinned Shortening Following a Thick-skinned Basement-involved Faulting in the Zagros Fold-thrust Belt

Zelong Guo[1,2], Mahdi Motagh[1,2], Jyr-Ching Hu[3], Guangyu Xu[4], Mahmud Haghshenas Haghighi[2], Abbas Bahroudi[5] and Aram Fathian[6]

[1]GFZ German Research Centre for Geosciences, Department of Geodesy, Section of Remote Sensing,14473 Potsdam, Germany

[2]Institute for Photogrammetry and GeoInformation, Leibniz University Hannover, 30167 Hannover, Germany

[3]Department of Geosciences, National Taiwan University, 10617 Taipei, Taiwan

[4]Faculty of Geomatics, East China University of Technology, 330013 Nanchang, Jiangxi, China

[5]Exploration Department, School of Mining Engineering, Engineering Faculty, University of Tehran, 515-14395 Tehran, Iran

[6]Neotectonics and Natural Hazards Institute, RWTH Aachen University, 52064 Aachen, Germany

Corresponding author: Zelong Guo (zelong.guo@gfz-potsdam.de)

Key Points:

- Coseismic deformation favors a planar fault model compared with listric fault models
- Kinematic afterslip explains postseismic deformation well, while stress-driven afterslip underestimates the early postseismic deformation
- Both thick- and thin-skinned shortening may be contributed by the 2017 Mw 7.3 Sarpol-e Zahab earthquake seismically and aseismically

Abstract

We use interferometric synthetic aperture radar (InSAR) observations to investigate the fault model and afterslip evolution within 3 years after the 2017 Sarpol-e Zahab, Iran, Mw 7.3 earthquake. The anti-listric fault which is very similar to flat-and-ramp structure inverted by kinematic afterslip models is proposed to simulate the coseismic slip and afterslip evolution. Compared with listric faults, linear inversions demonstrate that a planar fault can explain coseismic deformation well enough. However, the stress perturbations caused by this basement-involved faulting propagated upward to the sedimentary cover. The transition of sedimentary cover-basement interface inferred by afterslip models is at the depth of ~13 km in the seismogenic zone, which coincides with the regional stratigraphic profile and indicates that the significant afterslip updip of the coseismic rupture is mainly controlled by frictional property. We additionally find the postseismic deformation is dominated by afterslip while the

viscoelastic response is negligible with the best-fitting viscosity which is on the order of 10^{19} Pa s. Compared to the best-fitting kinematic afterslip model, the stress-driven afterslip model tends to underestimate early postseismic deformation to the west, which may indicate the spatial heterogeneity of the frictional property of fault plane. Because the coseismic rupture propagated along a basement-involved fault while the postseismic slip was likely to activate the frontal structures and/or shallower detachments in the sedimentary cover, the 2017 Sarpol-e Zahab earthquake may act as a typical event which contributes to both of the thick- and thin-skinned shortening of the Zagros in both seismic and aseismic way.

Plain Language Summary

The 2017 Mw 7.3 Sarpol-e Zahab earthquake is the largest instrumentally recorded event to have ruptured in the Zagros fold-thrust belt. Despite much work have done for a better understanding of the relation between crustal shortening and seismic and aseismic slip of the earthquakes in the Zagros, active debate remains. Here, we use InSAR observations to study the coseismic model and afterslip evolution within 3 years after the 2017 Mw 7.3 Sarpol-e Zahab earthquake. Our results suggest that coseismic planar model can fit the observations better than a range of listric faults. For postseismic deformation sources, afterslip and viscoelastic relaxation are considered to be possible causes of the postseismic deformation. Our results show that the kinematic afterslip model can explain the postseismic deformation spatiotemporally. However, the stress-driven afterslip model tends to underestimate the earlier western part of the postseismic deformation, which may indicate the spatial heterogeneity of frictional property of fault plane. Postseismic slip on more complex geological structures may also be reactivated and triggered, combined with geodetic inversions, geological cross-section data and local structures in the Zagros. We additionally find the viscoelastic response is negligible with the best-fitting viscosity.

1 Introduction

The ongoing collision between the Eurasian and Arabian Plate has led to the formation of one of the most tectonically and seismically active intra-continental orogens: the northwest-southeast striking Zagros mountain in southwestern Iran. The convergence velocity between Eurasian and Arabian Plate is ~2 to 3 cm yr^{-1}, almost half of which is accommodated by the Zagros mountain belt (Figure 1a; e.g., Vernant et al., 2004; Khorrami et al., 2019). In northwestern Zagros, the deformation rate is partitioned as ~5 mm yr^{-1} of dextral strike-slip motion along northwest-southeast trending faults and ~4 mm yr^{-1} of shortening perpendicular to the mountain belt, while in southeastern Zagros the deformation is ~9 mm yr^{-1} pure shortening perpendicular to the belt (Walpersdorf et al., 2006). Contemporary active deformation around the Zagros Fold-Thrust Belt (ZFTB) is mainly derived by seismic and aseismic deformation triggered by thrust and strike-slip faulting (e.g., Barnhart & Lohman, 2013; Motagh et al., 2015; Copley et al., 2015), folding and uplift of sedimentary cover (e.g., Berbe-

rian et al., 1995), and ductile thickening of the basement (Allen et al., 2013). The Phanerozoic sedimentary cover rock is ~8 to 13-km-thick, overlaying the Phanerozoic crystalline basement. A lot of work has been done to explore thin- and thick-skinned shortening related to the Phanerozoic sedimentary succession and deep basement faulting in the Zagros belt (e.g., Falcon 1969; Talebian & Jeckson, 2004; Molinaro et al., 2005; Mouthereau et al., 2012). Moderate magnitude earthquakes (~M 5-6) are widely distributed in ZFTB, but characterization and contribution of such seismicity in cover-basement interaction are still not fully understood (e.g., Talebian & Jeckson, 2004; Nissen et al., 2011; Motagh et al., 2015; Copley et al., 2015). A Hormuz salt unit in Fars Arc and shales in the Lurestan Arc due to the strong mechanical contrast between sedimentary cover and basement are suspected as a decoupling layer at the cover-basement interface (e.g., McQuarrie, 2004; Alavi, 2007), which may impede propagation of fault ruptures to the surface in this region. Under such geological and tectonic environment, many blind thrust faults which cut through the sedimentary cover, grow in ZFTB and contribute to the current topography of the Zagros. The major faults within ZFTB consist of the Main Recent Fault (MRF), the Mountain Front Fault (MFF), the High Zagros Fault (HZF) and the Zagros Foredeep Fault (ZFF) (Berberian 1995, Figure 1b).

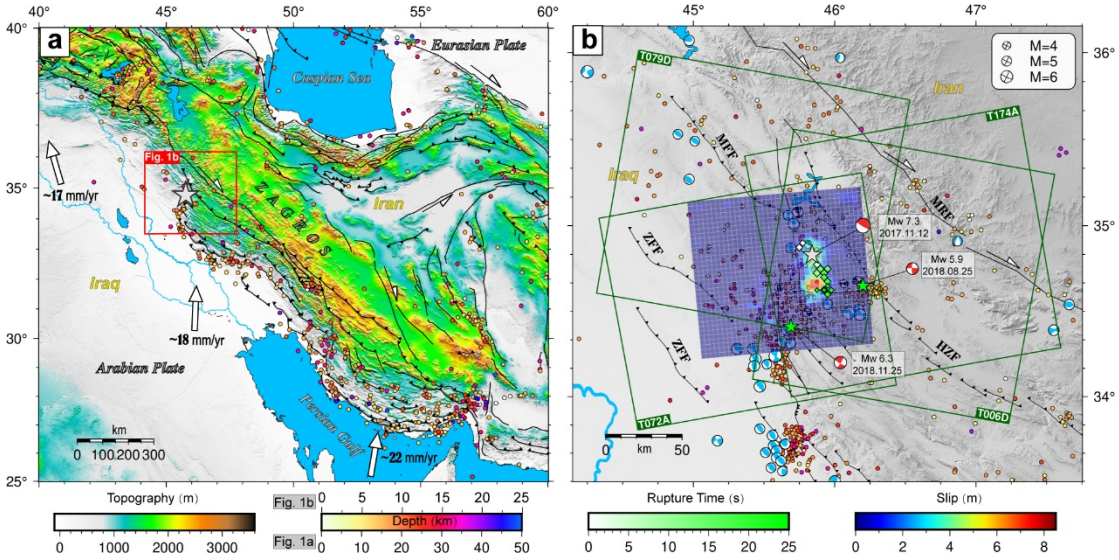

Figure 1. (a) Tectonic background of the 2017 Sarpol-e Zahab earthquake. The colored dots are earthquakes (from 1976 to 2021) from Global Centroid Moment Tensor (GCMT) catalogue (https://www.globalcmt.org). (b) Detailed tectonic map of the seismogenic area. The blue beach balls are from GCMT catalogue. Colored dots are earthquakes (from 2006 to 2021 with M > 3.5) from Iranian Seismological Center (IRSC, http://irsc.ut.ac.ir). Dark green boxes indicate the spatial extent of Sentinel-1 imagery used in this study. The coseismic slip distribution is given with the anti-listric fault model. Black beach balls are

from Nissen et al. (2019). Red beach balls are the focal mechanisms of 2017 Sarpol-e Zahab mainshock and two smaller aftershocks. The green rhombuses represent the rupture time of the mainshock, which is mapped from Nissen et al. (2019). ZFF: Zagros Foredeep Fault; MRF: Main Recent Fault; HZF: High Zagros Fault; MFF: Mountain Front Fault.

On 12 November 2017 at 18:18 UTC, an earthquake with magnitude of Mw 7.3 and focal depth about 21 km struck ~50 km north of Sarpol-e Zahab city, in Kermanshah province of western of Iran, which is also very close to the Iran and Iraq border (Figure 1). The main event occurred along a shallowly east-dipping reverse fault with dextral components in the Lurestan Arc of ZFTB and is the largest earthquake in this region since the instrumental records. Several ~M 6 earthquakes in the sedimentary cover followed the mainshock such as the 25 August 2018 Mw 5.9 event and 25 November 2018 Mw 6.3 event (Figure 1b). However, these two smaller aftershocks along steeply dipping dextral strike slip faults may reveal the strain partitioning in northwestern Zagros belt as the overall convergence direction between the Eurasian and Arabian Plate changes from orthogonal shortening in southeastern Zagros to oblique shortening in northwestern Zagros (e.g., Talebian & Jeckson, 2004). The 2017 Sarpol-e Zahab mainshock is located in crystalline basement, where the seismicity interactions between sedimentary cover and basal basement due to the possible existence of the weak Hormuz shale as a decoupled layer is still an open question (e.g., Nissen et al., 2011; Barnhart et al., 2018; Wang & Bürgmann, 2020).

Several studies have been done for a better understanding of seismic and aseismic slip of the 2017 Sarpol-e Zahab earthquake using geodetic observations (e.g., Barnhart et al., 2018; Chen et al., 2018; Feng et al., 2018; Vajedian et al., 2018; Yang et al., 2018; Nissen et al., 2019; Wang & Bürgmann, 2020; Lv et al., 2020; Fathian et al., 2021), but some debate still remains. In this study, we extend earlier studies and investigate both co and postseismic models of 2017 Mw 7.3 Sarpol-e Zahab event with interferometric synthetic aperture radar (InSAR) data. Firstly, we analyze the optimal coseismic fault model from planar and a range of listric faults with coseismic interferograms. Then we process ~3 years of Sentinel-1 data to derive the postseismic deformation time series and study the fault geometry and transient aseismic slip evolution for the first 4, 7, 10, 12, 24, and 36 months after the mainshock. Finally, we discuss about fault frictional heterogeneity, the reactivation of the Mountain Front Fault system and shallower multiple detachments that were most likely triggered by the mainshock, given our inversion results and the structural geology background of the Zagros.

2 InSAR observations

2.1 Data analysis

Four tracks of Sentinel-1 single look complex (SLC) data cover the seismogenic zone of the 2017 event (Figure 1b). The SLC data from two ascending tracks (T072A and T174A) and two descending tracks (T006D and T079D) is processed with GAMMA software (Wegmüller et al., 2015). The topography effect is

removed by a 30-meter (1 arc sec) Digital Elevation Model (DEM) from Shuttle Radar Topography Mission (SRTM; Farr et al., 2007). A 10 by 2 multi-look factor for range and azimuth direction is performed to improve the signal to noise ratio. Generic Atmospheric Correction Online Service for InSAR (GACOS) products (Yu et al., 2018) are used for reducing atmospheric delay error from differential interferograms (Table S1, Figure S1). The full variance-covariance matrix (VCM) constructed using a 1-D exponential covariance function with far-field nondeforming area in coseismic interferograms (Feng et al., 2013) indicates that the far-field noise is less than 1 cm after atmospheric delay correction with GACOS.

To analyze postseismic deformation, we perform multi-temporal interferometry analysis in four tracks of Sentinel-1 data based on Small Baseline Subset (SBAS) technique (Berardino et al., 2002). We construct a network of high-coherence small baseline interferograms covering 3 years after the 2017 Sarpol-e Zahab earthquake (Table S2). The thresholds of 50 meters and 200 days are selected for the spatial and temporal baselines in the SBAS analysis (Figure S2). A modified version of StaMPS software (Hooper et al., 2007) is used for time series analysis after differential interferometric processing with GAMMA. The measurement points are selected using a coherence threshold of 0.3. After correcting for the atmospheric delay using GACOS products and the DEM errors, we finally get the InSAR time series and cumulative line-of-sight (LOS) displacements for 3 years following the 2017 event.

2.2 Co and postseismic displacements

Coseismic interferograms from ascending data T072A and T174A suggest that the maximum and minimum LOS displacements are about 85 cm and -21 cm, respectively (surface motion toward the satellite is positive, Figure S1). For the descending data T006D and T079D, the maximum and minimum LOS displacements are about 50 cm and -39 cm, respectively (Figure S1). The difference in the sense of range measurements between ascending and descending tracks indicates significant contribution from east-west coseismic deformation. The coseismic interferograms also contain information from early postseismic deformation because of Sentinel-1 satellite 12-day revisit time.

As is shown in Figure 2e-f, the 3-year cumulative range changes at P1 and P2 are about 15 cm and -12 cm for ascending track T072A and descending track T006D, respectively. Note in Figure 2a-d, there are some localized signal contaminations due to the co and postseismic deformation of the two smaller aftershocks: the Mw 5.9 earthquake on 25 August 2018 and the Mw 6.3 earthquake on 25 November 2018 (Figure 1b and Figure 2a-d). In this study, the fault models of these two aftershocks proposed by Fathian et al. (2021) (Figure 2a-d and Figure S3) are used for forward modeling and then we made the difference between our original InSAR time series and the simulations to get a cleaner postseismic time series (Figure S3 and Figure S4). In the following sections, the coseismic deformation of the two aftershocks have been reduced from all of the time series influenced by these two smaller events (Figure S4)

and then employed for further analysis and inversions.

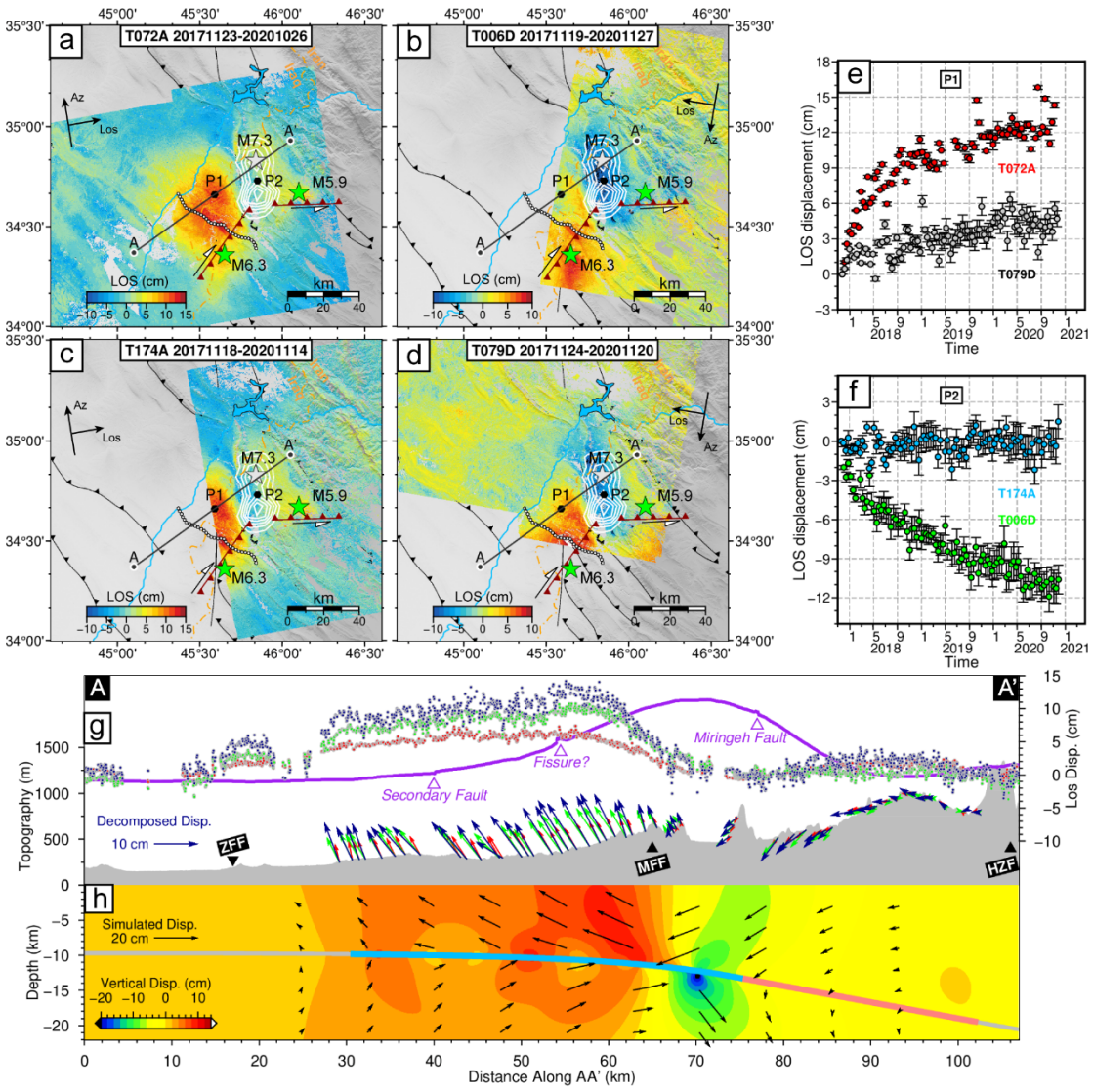

Figure 2. (a-d) represent the 3-year InSAR time series results from T072A, T006D, T174A and T079D, respectively. White contours and gray star represent our preferred coseismic slip model at 1-m intervals and the epicenter of the Mw 7.3 mainshock, separately. Green stars and dark red faults represent the locations of the two smaller aftershocks and the corresponding fault traces from Fathian et al. (2021). White dots are the surface trace of the secondary fault indicated by the coseismic interferogram discontinuity and filed survey (Vajedain et al., 2018). Profile AA' which is nearly orthogonal to the geological structures corresponds to the surface observations and simulations of Figure 6. Figure(e-

f) are the LOS displacement time series of P1 and P2, the error bars are the standard deviations from pixels within a radius of 30 meters. (g) shows the contribution of postseismic deformation to topography growth along profile AA'. The red, green and dark blue dots represent the postseismic LOS displacements of 3 months, 1 year and 3 years after the mainshock, respectively. The purple line indicates the coseismic LOS displacements which are scaled by a factor of 5. The red, green and dark blue vectors are the 2.5-dimension deformation (quasi-eastward and quasi-upward) of 3 months, 1 year and 3 years after the mainshock, separately, which are decomposed from ascending track T072A and descending track T079D. (h) shows the 3-dimension displacements in depths along profile AA', which is simulated from the 3-year kinematic afterslip model. The gray line indicated the anti-listric fault proposed in Section 4.1, the light red and light blue lines show the approximate scopes of coseismic rupture and postseismic afterslip, respectively. ZFF: Zagros Foredeep fault; HZF: High Zagros Fault; MFF: Mountain Front Fault.

3 Coseismic fault models

The four coseismic interferograms (Figure S1) are downsampled with quadtree sampling approach (Jónsson et al., 2002, Figure S5) to reduce the computation and then the nonlinear global search is performed for the fault parameters (Text S1 and Figure S6). After that, we carry out linear inversions for the distributed slip on the fault plane. The fault geometry derived from nonlinear inversion was fixed and we extended along-strike fault length to 100 km and along-downdip fault width to 90 km, before the fault plane is discretized to fault patches with 3 km by 3 km. Initially, we found that the fault model with a dip angle of 15° fits the coseismic displacements best from a variety of planar faults (Figure S7). We impose rake constraints from 110° to 160° and select 0.8 as the best-fitting smooth factor for the planar fault (Figure S7). In this study, we defined misfit as $misfit = \|W(Gs - d)\|_2$, in which W is the weight for different data, adopted to be equal for four tracks of InSAR observations; G is the Green's function (surface displacements of unit slip on fault plane); s and d are the fault slip and InSAR observations, respectively.

Fathian et al. (2021) proposed a listric fault to model coseismic deformation based on the relocated aftershocks even though other studies used a simply planar fault only (e.g., Feng et al., 2018; Barnhart et al., 2018; Wang & Bürgmann, 2020). Here, different from Fathian et al. (2021), we searched for the best listric fault model from the perspective of coseismic data fitting. We fix the upper fault depth at 13.4 km which is derived from our nonlinear inversion and then test a range of dip angles from 13° to 25° (hereafter called the initial dip) at this depth. We construct the following equation to constrain the fault:

$$\mathrm{dip}_n = \begin{cases} a \bullet (13.4 - n) + \mathrm{dip}_{n+1}, n < 13.4 \\ b,\ n = 13.4 \\ -a \bullet (n - 13.4) + \mathrm{dip}_{n-1}, n > 13.4 \end{cases}, b \in [13, 25] \quad (1)$$

where n is depth (km) of fault patch; dip_n represents the dip angle of fault patch

at the depth of n km; a controls the curvature of the fault model ($a \in [0 : 0.2 : 8]$), b is the initial dip of the nonlinear-inversion upper fault boundary where the depth is 13.4 km. Here we test a range of initial dips for b from 13-25° with 1° intervals. A particular case is that the fault would be planar and the dip angle would be b if $a = 0$. The same smoothing factor and rake constraints with abovementioned planar fault are imposed in the inversions. Our results show that, however, the best-fitting fault model is still a single planar fault dipping 15°, which can explain the InSAR observations well enough (Figure 3a). Even though the coseismic slip does not favor a listric model, this scenario cannot be ruled out considering potential postseismic slip may be reactivated on the Mountain Front Fault system (see Section 5.4).

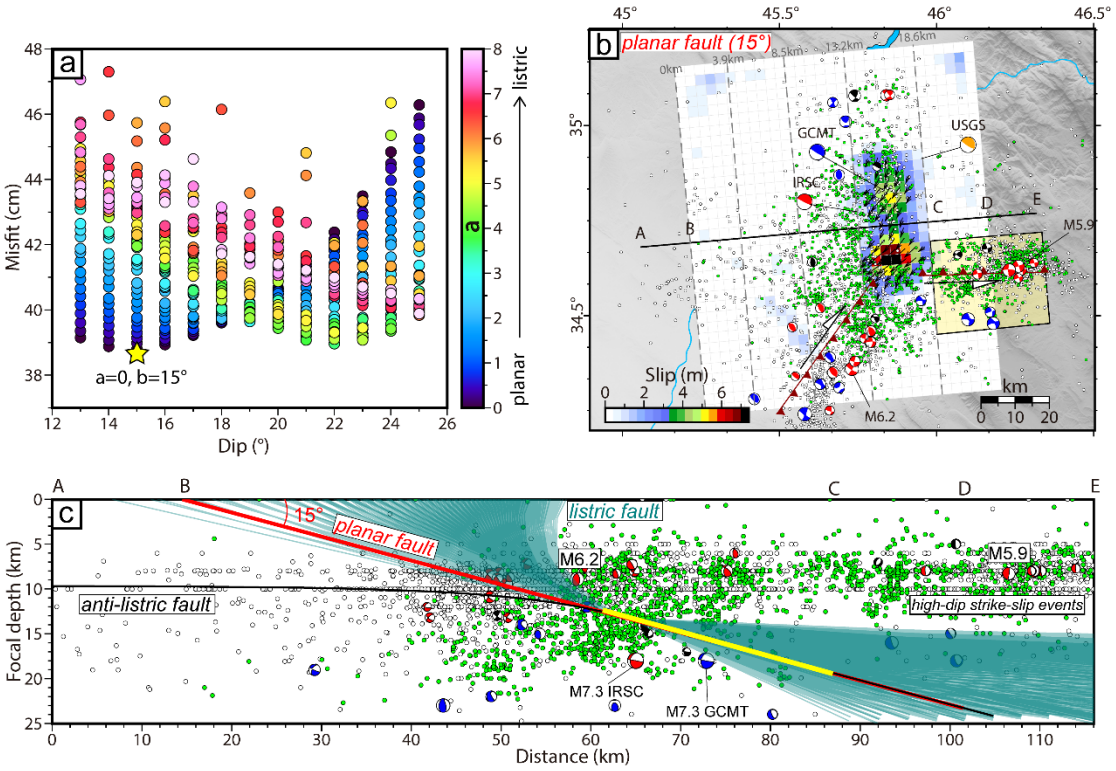

Figure 3. (a). The searched fault models with Equation (1). The optimal fault (yellow star) is a planar fault with dipping 15°. (b) Slip distribution with the planar fault dipping 15°. The two dark red, strike-slip faults of M 5.9 and M 6.3 events are from Fathian et al. (2021). The transparent yellow box indicates the likely cluster of strike-slip aftershocks. (c) is the seismicity projection of profile AE in (b) along depth. The green and white dots indicate the relocated aftershocks within about 2 months from Fathian et al. (2021) and aftershocks within about 3 years from IRSC catalogue, respectively. The red, blue and black beach balls are the focal mechanisms from IRSC, GCMT and Nissen et

al. (2019), respectively. The cyan lines indicate all of the tested listric fault models. The red and black lines are the planar fault model dipping 15° and the anti-listric model proposed in Section 4.1, respectively. The yellow line indicates the main coseismic rupture.

The coseismic slip model reveals a unilaterally southward rupture for the mainshock involving sequential rupture of two asperities, along a dextral-thrust fault (Figure 3b). The main coseismic slip area is concentrated at a depth range of ~13-19 km with maximum slip exceeding 7 m. The geodetic moment is estimated to be 1.0×10^{20} Nm, corresponding to a moment magnitude of Mw 7.3. Surface deformation predicted by the coseismic model is in good agreement with the observations (Figure S8). Our coseismic model reveals two asperities (Figure 3b), which is similar with the InSAR-derived results of some of previous studies (e.g., Barnhart et al., 2018; Feng et al., 2018), while others proposed only one simple asperity (e.g., Wang & Bürgmann, 2020). It is worth noting that a finite fault model from seismic waveforms and backprojection results also favor two apparent parts which produced separate peak slips and energy release (Nissen et al., 2019, Figure 1b). The difference between these studies may be attributed either to the low resolving ability of InSAR modeling or the difference of fault parameterization and inversion configurations in different studies.

4. Postseismic fault models

In this section, we explore the fault structure based on kinematic afterslip inversions and search for an optimal stress-driven afterslip model based on 4-, 7-, 10-month and 1-, 2-, 3-year postseisimic deformation. Then we explore the possibility of the combination of stress-driven afterslip and viscoelastic relaxation as the possible postseismic model. Here we did not take the poroelastic rebound into consideration because the predicted poroelastic contribution 1 year after the 2017 mainshock is lower than 5 mm and the spatial pattern of simulations is contrast to the postseismic observations (Wang & Bürgmann, 2020).

4.1 Fault model based on kinematic afterslip

Previous studies suggest that postseismic deformation of 2017 Sarpol-e Zahab event is mainly dominated by afterslip, while the viscoelastic and poroelastic contributions are negligible (Barnhart et al., 2018; Wang & Bürgmann 2020). Under such assumptions, they indicated the mainshock and afterslip activated a flat-and-ramp structure. Here, we perform more detailed searches than previous studies to derive the fault structures with postseismic deformation of 4, 7, 10, 12, 24 and 36 months after the mainshock (Figure S4). We downsample the InSAR postseismic observations uniformly around the main deformation area (Figure S9) and seek a time-invariant fault geometry that is able to match the InSAR observations satisfactorily, given estimates of their uncertainties. Initially, we attempt to search for a flat-ramp-flat structure. We fixed the middle ramp part with dip angle 15°, the angles of updip and downdip flat are allowed to vary above and below a certain depth, respectively (hereafter called the updip and downdip transition depth). Our results indicate that a wide range of downdip

angles can fit the data equally well (Figure S10), which may indicate that either the downdip slip is not sensitive to the observations or there is no obvious slip around there. From the 2-month relocated aftershocks (Fathian et al., 2021) and 3-year data from IRSC aftershock catalog (Figure 3b-c), we notice that the cluster of aftershocks east of the main slip area is mainly due to a shallower strike-slip faulting according to the focal mechanisms (transparent yellow box in Figure 3b), which is likely to be relevant to the causative fault plane of the 2018 August Mw 5.9 earthquake. Thus, the inadequacy of thrust events downdip of the fault may indicate that there is no clear postseismic afterslip along downdip direction as afterslip is one of the possible physical models to explain aftershock triggering (e.g., Hsu et al., 2006; Perfettini & Avouac, 2007).

For the updip geometry, the results show the updip angle should be lower than 15°, but the data have little resolution for the transition depth and dip angles smaller than 15° (Figure S10). To control the number of the variables and reduce the impact of downdip geometry to updip part, we also fix the downdip angle to 15° so that there are only two variables (updip angle and transition depth), and we re-search updip angle and transition depth. However, the result (Figure 4) found to be similar to the searching results of four variables (Figure S10). Therefore, the updip angle should be lower than 15° but the refined structure of updip geometry cannot be resolved well with InSAR observations. Interestingly, the upper transition depth is found to be about 13 km or 5-10 km. Such discrepancy may be due to the data and model errors, or indeed triggered postseismic slip on more complex geological structures considering the geological background and local stratigraphic profile, we will discuss it in the Section 5.4.

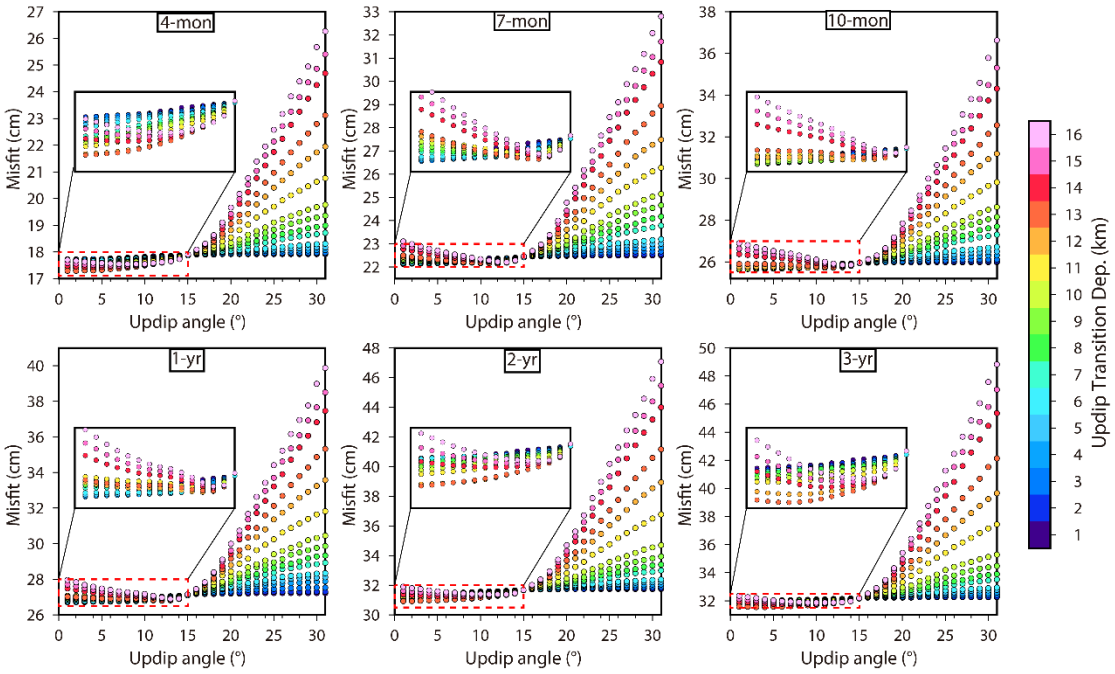

Figure 4. Misfit for searching the updip angles and transition depths with the postseismic observations of 4, 7, 10 months and 1, 2, 3 years after the mainshock.

Because it is difficult to make a compromise between updip angle and upper transition depth, we propose an anti-listric fault model with dip-variable at depth with the following equation, given the depth of basal decollement:

$$\mathrm{dip}_n = \begin{cases} -4 \bullet (13.4 - n) + \mathrm{dip}_{n+1}, n < 13.4 \\ 15, n \geq 13.4 \end{cases} \quad (2)$$

the symbols used and the meanings are same with Equation (1). We adopted $a = -4$ (the dip angle would be 0 at ~10 km) since the basement depth is about 8-13 km. What is more, this anti-listric fault is consistent with the aftershock locations updip of the coseismic rupture (Figure 3c) and this model strongly resembles the flat-and-ramp structure proposed by Barnhart et al. (2018) and Wang and Bürgmann (2020). The anti-listric model can not only explain the postseismic deformation but also produce slightly smaller misfit (38.3 cm) for coseismic inversion than the planar model (38.9 cm). Therefore, we take the anti-listric coseismic model (Figure S11) as our preferred one in the following inversions.

As is shown in Figure 5, the afterslip model based on the anti-listric fault mainly concentrated on updip of the coseismic rupture, despite some localized deep afterslip. The spatiotemporal evolution of kinematic afterslip model agrees well with the aftershock locations updip of the fault, which indicates the aftershocks may be triggered by aseismic afterslip. The maximum kinematic afterslip is

about 1.2 m. The cumulative moment release calculated from 3-year aftetslip model is about 2.6×10^{19} Nm, which is equivalent to the moment of a Mw 6.9 earthquake. The kinematic afterslip model can predict the InSAR observations well spatiotemporally (Figure 6).

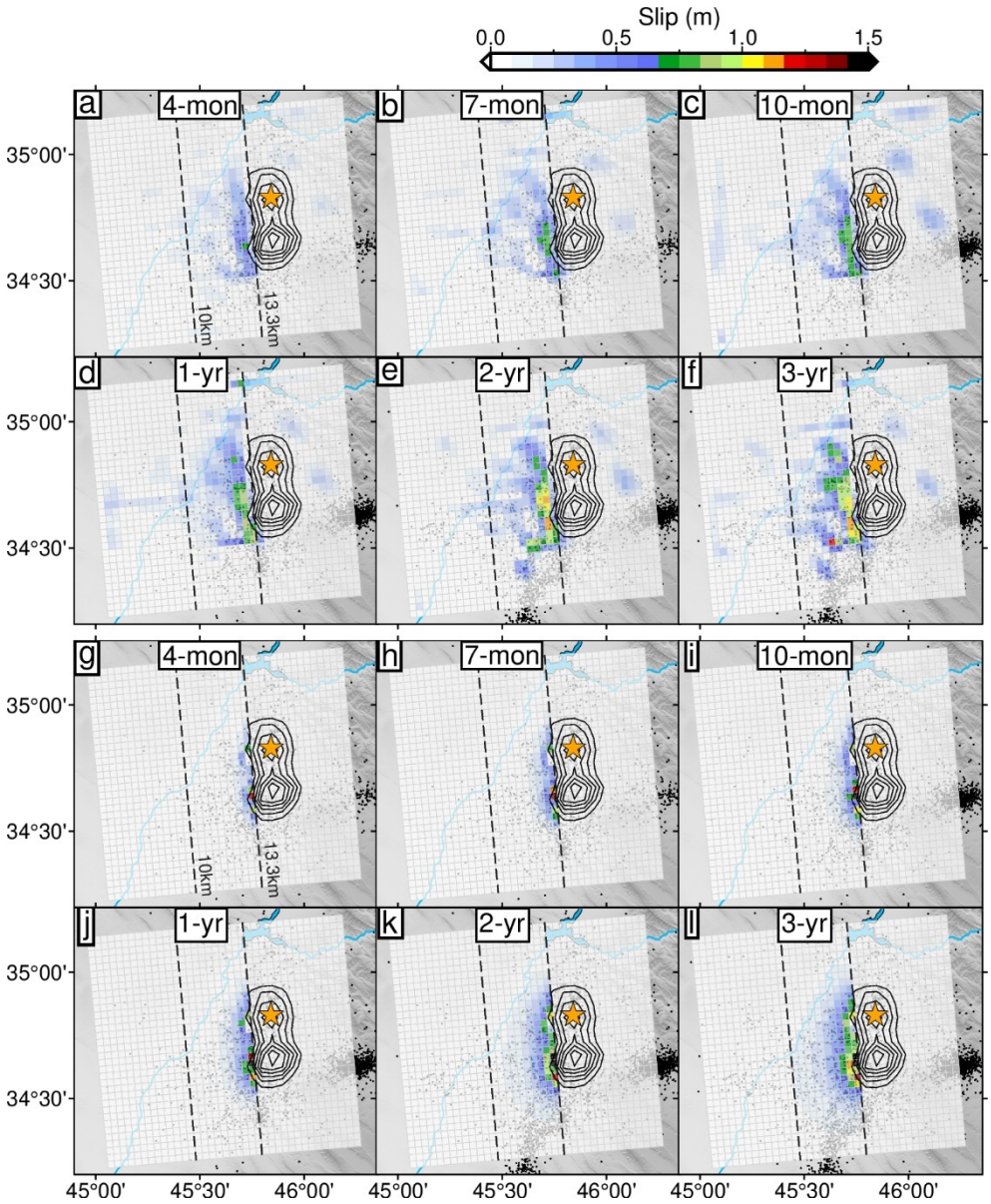

Figure 5. Spatiotemporal evolution of aftershocks, kinematic afterslip (a-f) and stress-driven afterslip (g-l). Black contours and orange star represent the coseismic slip model at 1-m intervals and the epicenter of the Mw 7.3 mainshock,

respectively. The black dots indicated the aftershocks are from IRSC catalogue. The black dashed lines represent the fault depth.

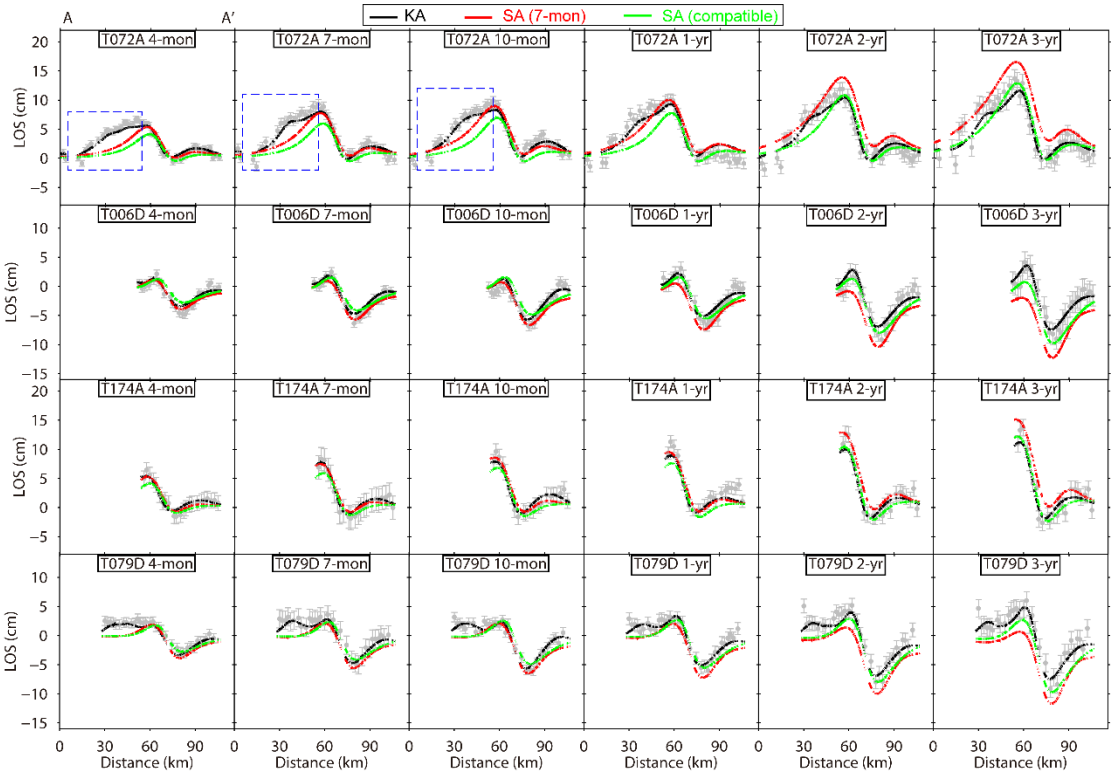

Figure 6. The fitting between InSAR observations and simulations from 4 months to 3 years after the mainshock along profile AA' in Figure 2a-d. The gray error bars are the InSAR observations, which represent the far-field noises from VCM. The black, red and green lines represent the simulations from kinematic afterslip (KA), stress-driven afterslip based on the 7-month postseismic deformation (SA 7-mon) and the compatible stress-driven afterslip based on the 4-month to 3-year postseismic deformation (SA compatible). The blue dashed boxes indicate the underfitting between observations and simulations from stress-driven afterslip.

4.2 Stress-driven afterslip simulation

We calculate the time-dependent evolution of rate-strengthening friction faults to coseismic stress change with the application of Unicycle codes (Barbot et al., 2017). Fault slip rate controlled by a purely rate-strengthening friction law can be shown as (e.g., Barboot et al., 2009):

$$V = 2V_0 \sinh \frac{\tau}{(a-b)\sigma} \quad (3)$$

this is a steady state simplification of the rate-and-state friction law (e.g.,

Marone et al., 1991; Marone 1998), where V_0 and $a-b$ represent the reference slip rate and frictional parameter of the material, τ and σ are the fault shear stress changes and the effective normal stress due to the earthquake. Note here V_0 does not correspond directly to the interseismic slip rate (Barboot et al., 2009). The steady state assumption is valid as the magnitude of the afterslip for the 2017 Sarpol-e Zahab earthquake ($> 10^{-1}$ m) is greater than the laboratory-derived values of D_c which is on the order of 10^{-5} m (e.g., Marone, 1998). In our simulations, we select the main coseismic area at the depth of ~12-20 km with coseismic slip > 0.8 m as Unicycle input model. The V_0 and $(a-b)\sigma$ considered as constitutive parameters are searched, based on the misfit between InSAR observations and simulations.

We search five parameters including V_0 and $(a-b)\sigma$ updip and downdip of the coseismic rupture and additionally, the transition depth where the fictional properties of fault rocks changes. Initially, the 7-month postseismic deformation from four tracks of Sentinel-1 images is used for searching the five parameters for two reasons: (1) the viscoelastic relaxation (if it is one of the dominant mechanisms) is smaller within the first 7 months than 3 years; (2) there is no signal contaminations of co and postseismic deformation of the two smaller ~M 6 earthquake. We employ the simulated annealing algorithm to search the global optimal solutions of the constitutive parameters, but there is still possibility to get the local minima due to the complexity of the chosen parameters for simulated annealing. Thus, we perform a number of iterative operations with different chosen parameters of the algorithm, initial values and boundary constraints. The solution which yields minimum data misfit is selected as the finally optimal solution. The results are shown in Table 1 and Figure S12. This model requires afterslip downdip of the coseismic rupture to explain 7-month postseismic deformation, which is similar to the result of Wang and Bürgmann (2020). However, the afterslip although predicts 1-year postseismic observations relatively well, it overestimates 3-year postseismic deformation (Figure 6).

Table 1. Constitutive parameters derived from this study and previous work.

Postseismic data/Source	Updip flat	Downdip ramp	Transition Depth (km)		
	$(a-b)\sigma$ (MPa)	V_0 (m yr^{-1})	$(a-b)\sigma$ (MPa)	V_0 (m yr^{-1})	
7-month	0.58	0.12	2.1	0.015	12.
Compatible[a]	1.3	0.12	-	0	13
Wang and Bürgmann (2020)	2.7	1.42	0.073	0.06	-

[a] based on the postseismic deformation of 4, 7, 10, 12, 24 and 36 months after the mainshock.

Our purpose is to seek a rate-strengthening afterslip model that is capable to estimate the InSAR observations spatiotemporally. Thus, we then search a more compatible parameters with the same searching strategy, but based on 4-, 7-, 10-, 12-, 24-, 36-month postseismic deformation. We calculate the simulations at

different periods with the afterslip evolution, then the compatible constitutive parameters are determined based on the lowest misfit between observations and simulations of 4, 7, 10, 12, 24, 36 months after the mainshock. The results show that the updip V_0 and $(a-b)\sigma$ are 0.12 m yr^{-1} and 1.3 MPa, respectively; the optimal transition depth is about 13.0 km (Table 1; Figure 7) which is similar with the transition depth calculated with 7-month postseismic deformation. However, for the downdip part of the fault, the V_0 is convergent to 0 m yr^{-1}, which also makes it difficult for downdip $(a-b)\sigma$ to converge (Table 1; Figure 7). This also indicates that the strong property contrast between updip and downdip of coseismic rupture, and downdip afterslip is not necessary. Compared with the afterslip model derived from 7-month postseismic deformation, the compatible model can better explain the observations (Figure 6). We take this compatible result as the best stress-driven afterslip model for following analysis.

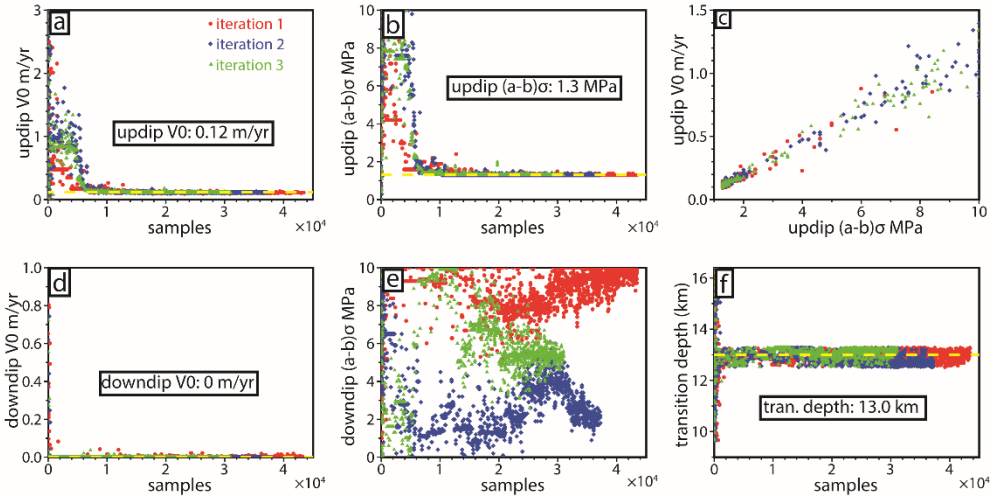

Figure 7. Convergence process with simulated annealing algorithms for V_0 and $(a-b)\sigma$ updip (a and b) and downdip (d and e) of the coseismic rupture, as well as the transition depth (f), based on the postseismic deformation of 4, 7, 10, 12, 24 and 36 months after the mainshock. The trade-off correlation between updip V_0 and $(a-b)\sigma$ are shown in (c). The yellow dashed line represents the optimal parameter.

4.3 The combination of stress-driven afterslip and viscoelastic relaxation

The contribution of viscoelastic relaxation is still in question: Wang and Bürgmann (2020) suggested that the viscoelastic relaxation deformation within 1 year is less than 1 cm, while Lv et al. (2020) argued that the viscoelastic contribution from 6 months to 2.5 years after mainshock is relatively significant. In this section, we attempt to explore a combined postseismic mechanism of viscoelastic relaxation and stress-driven afterslip. Based on the 7-month, 1-year and 3-year simulations from stress-driven afterslip model, we adopt PSCMP/PSGRN (Wang et al., 2006) to simulate the corresponding viscoelastic

relaxation using a layered elastic model and by exploring a range of Maxwell viscosities (from 1×10^{17} to 1×10^{20} Pa s). The same coseismic slip distribution used for inverting stress-driven afterslip is employed to calculate viscoelastic relaxation. We found that the best-fitting viscosity is about 10^{19} Pa s from these three models (Figure 8), which is consistent with the best estimates of the rheological viscosity from Lv et al. (2020). However, the viscoelastic response with a viscosity on the order of 10^{19} Pa s cannot match deformation pattern of ascending tracks (Figure S13). More importantly, the maximum range change of 3-year viscoelastic relaxation for descending tracks is about 1.5 cm (Figure S13), which is only about one tenth of the 3-year cumulative postseismic deformation. Our viscoelastic simulations are in a good agreement with Wang and Bürgmann (2020), indicating the viscoelastic relaxation is unlikely to be a dominant postseismic mechanism.

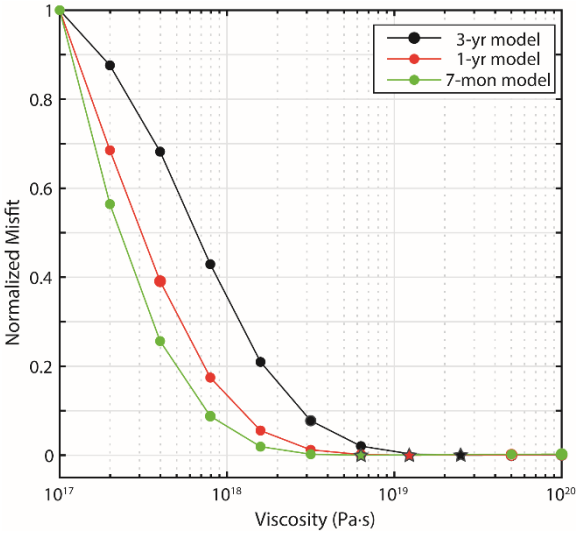

Figure 8. The trade-off between normalized misfit of 7-month, 1-year and 3-year postseismic observations and the viscosities. The green, red and black stars represent the best viscosity based on 7-month, 1-year and 3-year postseismic observations.

5. Discussion

5.1 Postseismic deformation and topography growth

The basement-involved faulting is found to significantly contribute to the topography growth and crustal shortening across the foreland of the mountain range via postsesimic deformation. The 2.5-dimension deformation fields decomposed from ascending track T072A and descending track T079D indicate a long-wavelength postseismic deformation (~80 km) along profile AA' (Figure 2a-d and g). The decomposed 2.5-dimension deformation is consistent with the simulations of kinematic afterslip model (Figure 2g-h), though the decom-

posed displacements neglect the south-north component because of the near-polar satellite orbits. In Figure 2g, postseismic deformation clearly contribute to the topography uplift western of Mountain Front Fault (from Zagros Foredeep Fault to Mountain Front Fault), while minor subsidence occurs east of the Mountain Front Fault (from Mountain Front Fault to High Zagros Fault). The westward movements across these faults highlight the aseismic contribution to the crustal shortening in the foreland of the Zagros. Such long-wavelength postseismic deformation may be related with the reactivation of regionally complex structures (also see Section 5.4).

5.2 Comparison with previous afterslip models

5.2.1 Kinematic afterslip models

The studies from Barnhart et al. (2018) and Wang and Bürgmann (2020) using about 4-month and 1-year postsesmic deformation, respectively, support a flat-and-ramp structure beneath the foreland of the Zagros. Both of the studies suggest significant afterslip concentrated on the shallow dipping (~1°-10°) flat updip of the coseismic rupture. In this study, we use 4-, 7-, 10-, 12-, 24- and 36-month postseismic data to search the postseismic fault structure. Our result confirms the dip angle of updip afterslip plane should be lower than 15° and the data have limited resolution for smaller dip angles. Interestingly, Barnhart et al. (2018) and Wang and Bürgmann (2020) indicate the optimal afterslip depth is about 10-14 km, which is also similar to our study as models in our study with transition depth at ~13 km yield minimum data misfit (Figure 4 and S10). However, our results also show the transition depth at 5-10 km is possible with searching of 7-month to 1-year postseismic deformation (Figure 4 and S10). The InSAR observations cannot resolve the updip angles and transition depths well enough because of the observation noises like residual atmospheric error, model regularization error as well as the complexity of the postseismic deformation sources. Therefore, the transition depth at 5-10 km may have large uncertainties due to data resolution, but it is also indeed possible that some postseismic slip occurs there considering the complicated mechanical stratigraphy of the Zagros (see Section 5.4).

5.2.2 Stress-driven afterslip models

Compared with four parameters searched by Wang and Bürgmann (2020) with Bayesian inversion, we searched five constitutive parameters of rate-strengthening afterslip model with simulated annealing algorithm. We take the compatible constitutive parameters based on 4-, 7-, 10-, 12-, 24- and 36-month postseismic deformation as the best-fitting model as it can explain the InSAR observations better than constitutive parameters searched with individually 7-month postseismic deformation (Figure 6). However, our preferred results are different from Wang and Bürgmann (2020). Based on the 1-year postseisic deformation, Wang and Bürgmann (2020) derived the best values of V_0 and $(a-b)\sigma$ to be 1.42 m yr^{-1} and 2.7 MPa for updip, 0.06 m yr^{-1} and 0.073 MPa for downdip part (Table 1). Both models from us in this study and the one by

Wang and Bürgmann (2020) indicate that the main afterslip occurred updip of the coseismic rupture. However, in contrast to Wang and Bürgmann (2020) we do not find significant afterslip downdip of the coseismic rupture.

Previous studies found that stress-driven afterslip model is relatively insensitive to $(a-b)\sigma$ compared with V_0, and the variation of $(a-b)\sigma$ would not affect the overall afterslip pattern (e.g., Xu et al. 2019). But the real physical meaning of V_0 may be rather complex (e.g., Barbot et al., 2009; Perfettini & Avouac, 2007). The magnitude of V_0 updip of the fault (1.42 m yr^{-1}) from Wang and Bürgmann (2020) is greater than ours (0.12 m yr^{-1}). Such a difference may partly result from the inconsistency of InSAR observations used for searching and trade-off of V_0 and $(a-b)\sigma$ (Figure 7c), which is also suggested by Wang and Bürgmann (2020). The trade-off between V_0 and $(a-b)\sigma$ is expected as equivalent V on the fault patches would be produced with low values of V_0 or high values of $(a-b)\sigma$ (see Equation 3). Compared with the model from Wang and Bürgmann (2020), we additionally take the spatiotemporal afterslip evolution of different postseismic stages into consideration to derive the most compatible results from various segments of InSAR time-series data. Overall, similar to Wang and Bürgmann (2020), our results reflect the significant frictional contrast between updip and downdip of coseismic rupture.

5.3 The location of afterslip and the contribution from viscoelastic flow

Afterslip is a rather complex physical process and has not been clearly understood yet. In the framework of rate-and-state friction law, the coseismic rupture usually initiates and propagates in the velocity-weakening area and its propagation tends to be impeded by the shallower unconsolidated sediments. This sediment layer with velocity-strengthening properties then would be strongly loaded and drives afterslip in consequence (Marone et al., 1991). At the downdip direction of the coseismic rupture in midcrustal depths, a transition of fault friction from velocity-weakening stick slip to velocity-strengthening brittle creep would be expected because the temperature gets higher with depth (e.g., Marone, 1998; Perfettini & Avouac, 2004). However, ductile flow may also be activated at depth (e.g., lower crust or upper mantle) where temperature gets higher enough to produce dislocation creep (Perfettini & Avouac, 2004). Overall, as predicted by rate-and-state dependent friction law, in most cases afterslip tends to occur at the periphery of the coseismic rupture, where slip deficit is left by mainshocks.

For some thrust earthquakes which share similar tectonic settings with the 2017 Sarpol-e Zahab earthquake like the 1999 Chi-chi, the 2005 Kashimir and the 2015 Gorkha earthquake, the significant afterslip occurred at the downdip portion of the fault, in conjunction with possible viscoelastic relaxation (e.g., Hsu et al., 2002; Wang & Fialko, 2014; Diao et al., 2021). However, little or no deep afterslip downdip of the coseismic rupture (Figure 5) is required by our kinematic and velocity-strengthening afterslip models for this 2017 Sarpol-e Zahab event; the viscoelastic response is also negligible as the optimal viscosity based on 7-month, 1-year and 3-year rate-strengthening afterslip models is on

the order of 10^{19} Pa s, which confirms the result from Wang and Bürgmann (2020). Prominent afterslip updip of the coseismic rupture from our afterslip models coincides with the strong frictional contrast between updip and downdip portion of the fault. Such frictional contrast may correspond to stratigraphic relations between sedimentary cover and crystalline basement (Figure 9). The transition depth from both of kinematic and rate-strengthening afterslip models is convergent to ~13 km which also agrees well with the Hormuz evaporites according to stratigraphic profiles of this region (Figure 9, e.g., Casciello et al., 2009; Vergés et al., 2011), indicating the possible depth of cover-basement interface. Chen et al. (2018) performed joint inversion using satellite radar and teleseismic data and found the coseismic rupture velocity is more rapid downdip (~3.2 km/s) of the fault than updip (~1.5 km/s), which supports the assumption that the mainshock ruptured the cover-basement interface and was impeded by the updip sedimentary rocks. Subsequently, the loose sediments with velocity-strengthening properties are more prone to drive afterslip (Marone et al., 1991). The existence of such low friction interface due to the transition between different geological units may be the reason that the spatial location of afterslip following the 2017 Sarpol-e Zahab event is different from other events shared similar tectonic settings.

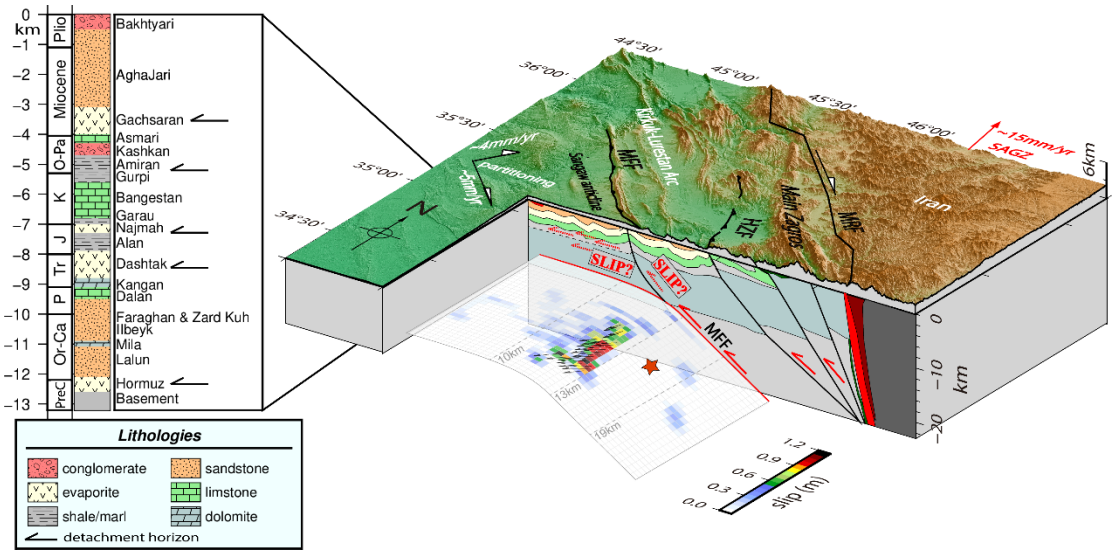

Figure 9. 3-D block diagram showing the tectonics, fault geometry, kinematic afterslip of 3 years after the mainshock and stratigraphic column in northwestern Zagros. The geological cross-section data is from National Iranian Oil company. The GPS velocity (SAGZ site) is from Khorrami et al. (2019). The simplified stratigraphic profile with approximate depths for Lurestan Salient is modified and referred from previous studies: Casciello et al., 2009; Vergés et al., 2011; Sadeghi & Yassaghi, 2016 and Le Garzic et al., 2019. Red star represents the epicenter of the 2017 Sarpol-e Zahab earthquake. Stratigraphy ages

and main faults are abbreviated as follows: Plio, Pliocene; O-Pa, Oligocene-Eocene-Palaeocene; K, Cretaceous; J, Jurassic; Tr, Triassic; P, Permian; Or-Ca, Ordovician-Cambrian; PreC, PreCambrian; MRF: Main Recent Fault; HZF: High Zagros Fault; MFF: Mountain Front Fault.

5.4 The early underfitting of stress-driven afterslip models

The geological structures of the seismogenic zone are rather complex. Multiple structures were triggered during the mainshock and can be seen from the coseismic interferogram discontinuities (Figure 2a-d and g; Feng et al., 2018; Vajedian et al., 2018; Wang & Bürgmann, 2020). For example, the secondary fault in Figure 2a-d and g is also verified by the filed survey (Vajedian et al., 2018). Under such tectonic background, the spatiotemporal pattern of postseismic slip for the 2017 Sarpol-e Zahab earthquake may be even further complex. As shown in Figure 6, for 3-year postseismic deformation, the rate-strengthening afterslip model can overall explain the InSAR observations well, but it tends to underestimate the earlier part of the postseismic deformation west of the deformation field for T072A (the blue dashed box in Figure 6). Such far-field underfitting is unlikely to attribute to the poroelastic rebound and viscoelastic relaxation, because the former mainly contribute to near-filed range changes (e.g., Peltzer et al., 1998) while the latter is negligible. The signal contamination from the two smaller aftershocks, i.e., the 2018 Mw 5.9 event and the Mw 6.3 event, can also be ruled out because it is far from the northwestern deformation area along profile AA' (Figure 2). Given our afterslip inversions, geological data and local structures, some inferences about this underfitting are discussed as follows:

5.4.1 The spatial heterogeneity of frictional property of fault plane

Compared with the stress-driven afterslip model, the kinematic afterslip model can explain the deformation spatiotemporally (Figure 6), which may indicate the spatial heterogeneity of frictional property of the fault rock. Such heterogeneity, which may also be reflected by the rake variations between the two coseismic rupture (Figure 3b), is not taken into the consideration in our velocity-strengthening inversions and in part lead to, if not entirely, the underfitting between postseismic observations and simulations.

5.4.2 The reactivation of the blind Mountain Front Fault

With the integration of geological field data, seismic reflection profiles and well data, Tavani et al. (2018) concluded that the 2017 mainshock ruptured along the blind Mountain Front Fault which also matches our geological cross section data well (Figure 9). The reactivated Mountain Front Fault and the inherited structures break through the basal basement to the sedimentary cover in the vicinity of the mainshock (Figure 9), and are supposed to be responsible for the multiple geological structures triggered during the mainshock, for example, the Miringeh fault (Tavani et al., 2018; Figure 2g). Such thrusting system is also considered as one of the folding mechanisms (e.g., McQuarrie 2004; Alavi, 2007) and has been constructed to model the anticline evolution on the top of Mountain Front Fault in Lurestan Arc (Emami et al., 2010). Thus, except for

the significant postseismic slip occurred on the cover-basement interface at the depth of ~13 km indicated by our kinematic and stress-driven afterslip models, the updip portion of the Mountain Front Fault or the inherited structures in sedimentary cover may also be reactivated by the mainshock and possible postseismic slip was triggered there (Figure 9).

5.4.3 Triggered slip on the shallower detachment horizons

Our kinematic afterslip models indicate another possible transition depth at ~5-10 km (Figure 4 and S10). The layered aftershocks between the depth of 5-10 km can also be seen in Figure 3c, indicating some aseismic slip may have occurred there. O'Brien (1950) firstly subdivided the Zagros vertical profile into five major structural units from shallow to deep: incompetent group, upper mobile group, competent group, lower mobile group and basement group. Even though the "competent group" at the depth of ~5-10 km was established by this mechanical stratigraphy, multiple weak detachment horizons, often of shales, marls or evaporites, are present from northwest to southeast of Lurestan salient (Figure 9; e.g., Casciello et al., 2009; Sadeghi & Yassaghi, 2016; Le Garzic et al., 2019). The weak sedimentary multi-layers in which the folds and thrust faults developed are prone to deform and directly control the distribution and process of the folds in this region (Casciello et al., 2009; Vergés et al., 2011). Thus, we suggest the rupture of the 2017 Sarpol-e Zahab earthquake may propagate across these decoupling horizons. A similar interpretation by Copley et al. (2015) was suggested for the 2014 Mw 6.2 Mormori earthquake in this region. The possible triggered postseismic slip on the local detachments (Figure 9) may further couple and contribute to the fold evolutions within the sedimentary cover. The structural interpretation for this assumption is that the stress changes due to the 2017 mainshock were not fully decoupled by the low friction interface (Hormuz unit) at the cover-basement transition, and then upward propagated into the incompetent detachment levels along Mountain Front Fault (Figure 9). Overall, the basement thrusting system may pierce into the Phanerozoic cover and multiple decoupling layers are involved and triggered by the mainshock (Figure 9). Thus, the two-layer decoupled model would be not enough to interpret the complex interaction between the thin-, thick-skinned shortening and the seismicity in the Zagros (e.g., Barnhart et al., 2018; Wang & Bürgmann, 2020). The 2017 Sarpol-e Zahab event may be regarded as a representative example in the Zagros which contributes to both of the thick- and thin-skinned shortening in seismic and aseismic way.

6. Conclusion

The 2017 Mw 7.3 Sarpol-e Zahab earthquake is the largest instrumentally recorded event to have ruptured in the ZFTB. To deepen the understanding of the relations between the seismic events and the crustal shortening in this region, the co and postseismic models associated with this event are studied with InSAR observations in this study. The main conclusions of this work are as follows:

(1) Linear inversions reveal a planar fault which is capable to explain the coseismic deformation better than the listric faults. The coseismic rupture highlights a unilaterally southward rupture involving sequential rupture of two asperities along a dextral-thrust fault.

(2) The kinematic afterslip model which can predict the postseismic deformation spatiotemperally supports a flat-and-ramp structure with the dip angle of the shallower flat lower than 15°. The optimal stress-driven afterslip model favors only afterslip occurred updip of the coseismic rupture and it tends to underestimate the early postseismic deformation. The transition depth inverted from kinematic afterslip and rate-strengthening afterslip models is about 13 km, which can be best explained by the cover-basement interface.

(3) The best-fitting viscosity based on combination mechanism of viscoelastic relaxation and stress-driven afterslip models is on the order of 10^{19} Pa s, at which the viscoelastic contribution to the postseismic deformation is negligible.

(4) The postseismic deformation contribute to the topography growth along vertical direction as well as the crustal shortening along the horizontal direction. The mismatch between the early postseismic deformation west of deformation field of T072A and stress-driven afterslip simulations can be explained either by spatial heterogeneity of frictional property of the fault rock or by triggered slip on more complex geological structures, e.g., the updip of Mountain Front Fault and the inherited structures, as well as the multiple detachment horizons there.

Acknowledgments

Zelong Guo gratefully acknowledge the scholarship supported him by China Scholarship Council (202006270005). Most of the figures were plotted with Generic Mapping Tools (GMT, Wessel & Smith, 1998) software. We thank the National Iranian Oil company for the geological cross-section data and Mohammad Tatar for the relocated aftershocks. Guangyu Xu has been funded by National Natural Science Foundation of China (42104008).

Data Availability Statement

The Sentinel-1 data is copyright of European Space Agency and provided by Alaska Satellite Facility (ASF, https://www.asf.alaska.edu). Aftershock data can be obtained from Iranian Seismological Center (IRSC, http://irsc.ut.ac.ir).

References

Alavi, M. (2007). Structures of the Zagros fold-thrust belt in Iran. *American Journal of Science, 307*, 1064–1095. https://doi.org/10.2475/09.2007.02

Allen, M. B., Saville, C., Blanc, E. J. P., Talebian, M., & Nissen, E. (2013). Orogenic plateau growth: Expansion of the Turkish-Iranian Plateau across the Zagros fold-and-thrust belt. *Tectonics, 32*, 171–190. https://doi.org/10.1002/tect.20025

Barbot, S., Fialko, Y., & Bock, Y. (2009). Postseismic deformation due to the

Mw 6.0 2004 Parkfield earthquake: Stress-driven creep on a fault with spatially variable rate-and-state friction parameters. *Journal of Geophysical Research, 114*, B07405. https://doi.org/10.1029/ 2008JB005748

Barbot, S., Moore, J. D. P., & Lambert, V. (2017). Displacement and stress associated with distributed anelastic deformation in a half-space. *Bulletin of the Seismological Society of America, 107*(2), 821–855. https://doi.org/10.1785/0120160237

Barnhart, W. D., Brengman, C. M. J., Li, S., & Peterson, K. E. (2018). Ramp-flat basement structures of the Zagros Mountains inferred from co-seismic slip and afterslip of the 2017 Mw7.3 Darbandikhan, Iran/Iraq earthquake. *Earth and Planetary Science Letters, 496*, 96–107. https://doi.org/10.1016/j.epsl.2018.05.036

Barnhart, W. D., & Lohman, R. B. (2013). Phantom earthquakes and triggered aseismic creep: Vertical partitioning of strain during earthquake sequences in Iran. *Geophysical Research Letters, 40*, 819–823. https://doi.org/10.1002/grl.50201

Berardino, P., Fornaro, G., Lanari, R., & Sansosti, E. (2002). A new algorithm for surface deformation monitoring based on small baseline differential SAR interferograms. *IEEE Transactions on Geoscience and Remote Sensing, 40*(11), 2375–2383. https://doi.org/10.1109/TGRS.2002.803792

Berberian, M. (1995). Master "blind" thrust faults hidden under the Zagros folds: Active basement tectonics and surface morphotectonics. *Tectonophysics, 241*, 193–224. https://doi.org/10.1016/0040-1951(94)00185-C

Casciello, E., Vergés, J., Saura, E., Casini, G., Fernández, N., Blanc, E., Homke, S., & Hunt, D. W. (2009). Fold patterns and multilayer rheology of the Lurestan Province, Zagros Simply Folded Belt (Iran). *Journal of the Geological Society, London, 166*, 947–959. https://doi.org/10.1144/0016-76492008-138

Chen, K., Xu, W., Mai, P. M., Gao, H., Zhang, L., & Ding, X. (2018). The 2017 Mw 7.3 Sarpol Zahāb Earthquake, Iran: A compact blind shallow-dipping thrust event in the mountain front fault basement. *Tectonophysics, 747–748*, 108–114. https://doi.org/10.1016/j.tecto.2018.09.015

Copley, A., Karasozen, E., Oveisi, B., Elliott, J. R., Samsonov, S., & Nissen, E. (2015). Seismogenic faulting of the sedimentary sequence and laterally variable material properties in the Zagros Mountains (Iran) revealed by the August 2014 murmuri (E. Dehloran) earthquake sequence. *Geophysical Journal International, 203*, 1436–1459. https://doi.org/10.1093/gji/ggv365

Diao, F., Wang, R., Xiong, X., & Liu, C. (2021). Overlapped postseismic deformation caused by afterslip and viscoelastic relaxation following the 2015 Mw 7.8 Gorkha (Nepal) earthquake. *Journal of Geophysical Research: Solid Earth, 126*, e2020JB020378. https://doi. org/10.1029/2020JB020378

Emami, H., Vergés, J., Nalpas, T., Gillespie, P., Sharp, I., Karpuz, R., Blanc, E. P., & Goodarzi, M. G. H. (2010). Structure of the Mountain Front Flexure

along the Anaran anticline in the Pusht-e Kuh Arc (NW Zagros, Iran): Insights from sand box models. *Geological Society, London, Special Publications, 330*, 155–178. https://doi.org/10.1144/SP330.9

Falcon, N. L. (1969). Problems of the relationship between surface structure and deep displacements illustrated by the Zagros Range. *Geological Society of London, Special Publications, 3*, 9–21. https://doi.org/10.1144/GSL.SP.1969.003.01.02

Farr, T. G., Rosen, P. A., Caro, E., Crippen, R., Duren, R., Hensley, S., et al. (2007). The shuttle radar topography mission. *Reviews of Geophysics, 45*, RG2004. https://doi.org/10.1029/2005RG000183

Fathian, A., Atzori, S., Nazari, H., Reicherter, K., Salvi, S., Svigkas, N., Tatar, M., Tolomei, C., & Yaminifard, F. (2021). Complex co- and postseismic faulting of the 2017–2018 seismic sequence in western Iran revealed by InSAR and seismic data. *Remote Sensing of Environment, 253*. https://doi.org/10.1016/j.rse.2020.112224

Feng, W., Li, Z., Elliott, J. R., Fukushima, Y., Hoey, T., Singleton, A., Cook, R., & Xu, Z. (2013). The 2011 Mw 6.8 Burma earthquake: fault constraints provided by multiple SAR techniques. *Geophysical Journal International, 195*, 650–660. https://doi.org/10.1093/gji/ggt254

Feng, W., Samsonov, S., Almeida, R., Yassaghi, A., Li, J., Qiu, Q., Li, P., & Zheng, W. (2018). Geodetic Constraints of the 2017 Mw7.3 Sarpol Zahab, Iran Earthquake, and Its Implications on the Structure and Mechanics of the Northwest Zagros Thrust-Fold Belt. *Geophysical Research Letters, 45*, 6853–6861. https://doi.org/10.1029/2018GL078577

Hooper, A., Segall, P., & Zebker, H. (2007). Persistent scatterer interferometric synthetic aperture radar for crustal deformation analysis, with application to Volcán Alcedo, Galápagos. *Journal of Geophysical Research, 112*, B07407. https://doi.org/10.1029/2006JB004763

Hsu, Y.-J., Bechor, N., Segall, P., Yu, S.-B., Kuo, L.-C., & Ma K.-F. (2002). Rapid afterslip following the 1999 Chi-Chi, Taiwan earthquake. *Geophysical Research Letters, 29*(16). https://doi.org/10.1029/2002GL014967

Hsu, Y.-J., Simons, M., Jean-Philippe, A., Galetzka, J., Sieh, K., & Bock, Y. (2006). Frictional Afterslip Following the 2005 Nias-Simeulue Earthquake, Sumatra. *Science, 312*, 1921–1926. https://doi.org/10.1126/science.1126960

Jónsson, S., Zebker, H., Segall, P., & Amelung, F. (2002). Fault slip distribution of the 1999 Mw7.1 Hector Mine, California, earthquake, estimated from satellite radar and GPS measurements. *Bulletin ofthe Seismological Society of America, 92*(4), 1377–1389. https://doi.org/ 10.1785/0120000922

Khorrami, F., Vernant, P., Masson, F., Nilfouroushan, F., Mousavi, Z., Nankali, H., Saadat, S. A., Walpersdorf, A., Hosseini, S., Tavakoli, P., Aghamohammadi, A., & Alijanzade, M. (2019). An up-to-date crustal deformation map of Iran

using integrated campaign-mode and permanent GPS velocities. *Geophysical Journal International, 217*, 832–843. https://doi.org/10.1093/gji/ggz045

Le Garzic, E., Vergés, J., Sapin, F., Saura, E., Meresse, F., & Ringenbach, J. C. (2019). Evolution of the NW Zagros Fold-and-Thrust Belt in Kurdistan Region of Iraq from balanced and restored crustal-scale sections and forward modeling. *Journal of Structural Geology, 124*, 51–69. https://doi.org/10.1016/j.jsg.2019.04.006

Lv, X., Amelung, F., Shao, Y., Ye, S., Liu, M., & Xie, C. (2020). Rheology of the Zagros Lithosphere from Post-Seismic Deformation of the 2017 Mw7.3 Kermanshah, Iraq, Earthquake. *Remote Sensing, 12*(2032). https://doi.org/10.3390/rs12122032

Marone, C. J., Scholtz, C. H., & Bilham, R. (1991). On the mechanics of earthquake afterslip. *Journal of Geophysical Research, 96*(B5), 8441–8452. https://doi.org/10.1029/91JB00275.

Marone, C. J. (1998). Laboratory-derived friction laws and their application to seismic faulting. *Annual Review of Earth and Planetary Sciences, 26*, 643–696. https://doi.org/10.1146/annurev.earth.26.1.643

McQuarrie, N. (2004). Crustal scale geometry of the Zagros fold-thrust belt, Iran. *Journal of Structural Geology, 26*, 519–535. https://doi.org/10.1016/j.jsg.2003.08.009

Molinaro, M., Leturmy, P., Guezou, J. C., Frizon de Lamotte, D., & Eshraghi, S. A. (2005). The structure and kinematics of the southeastern Zagros fold-thrust belt, Iran: From thin-skinnedned to thick-skinnedned tectonics. *Tectonics, 24*(TC3007). https://doi.org/10.1029/2004TC001633

Motagh, M., Bahroudi, A., Haghighi, M. H., Samsonov, S., Fielding, E., & Wetzel, H. U. (2015). The 18 August 2014 Mw 6.2 Mormori, Iran, Earthquake: A thin-skinnedned faulting in the zagros mountain inferred from InSAR measurements. *Seismological Research Letters, 86*(3), 775–782. https://doi.org/10.1785/0220140222

Mouthereau, F., Lacombe, O., & Vergés, J. (2012). Building the Zagros collisional orogen: Timing, strain distribution and the dynamics of Arabia/Eurasia plate convergence. *Tectonophysics, 532–535*, 27–60. https://doi.org/10.1016/j.tecto.2012.01.022

Nissen, E., Ghods, A., Karasözen, E., Elliott, J. R., Barnhart, W. D., Bergman, E. A., Hayes, G. P., Jamal-Reyhani, M., Nemati, M., Tan, F., Abdulnaby, W., Benz, H. M., Shahvar, M. P., Talebian, M., & Chen, L. (2019). The 12 November 2017 M w 7.3 Ezgeleh-Sarpolzahab (Iran) Earthquake and Active Tectonics of the Lurestan Arc. *Journal of Geophysical Research: Solid Earth, 124*, 2124–2152. https://doi.org/10.1029/2018JB016221

Nissen, E., Tatar, M., Jackson, J. A., & Allen, M. B. (2011). New views on earthquake faulting in the Zagros fold-and-thrust belt of Iran. *Geophysical Journal International, 186*, 928–944. https://doi.org/10.1111/j.1365-246X.2011.05119.x

O'Brien, C.A.E. (1950). Tectonic problems of the oil field belt of southwest Iran. In: BUITER, J. (ed.) Proceedings of 18th International Geological Congress, Great Britain, Part 6, 45–58.

Perfettini, H., & Avouac, J.-P. (2004). Postseismic relaxation driven by brittle creep: A possible mechanism to reconcile geodetic measurements and the decay rate of aftershocks, application to the Chi-Chi earthquake, Taiwan. *Journal of Geophysical Research, 109*(B02304). https://doi.org/10.1029/2003jb002488

Perfettini, H., & Avouac, J. P. (2007). Modeling aftership and aftershocks following the 1992 Landers earthquake. *Journal of Geophysical Research, 112*(B07409). https://doi.org/10.1029/2006JB004399

Peltzer, G., Rosen, P., Rogez, F., & Hudnut, K. (1998). Poroelastic rebound along the Landers 1992 earthquake surface rupture. *Journal of Geophysical Research, 103*(B12), 30131–30145. https://doi.org/10.1029/98JB02302

Sadeghi, S., & Yassaghi, A. (2016). Spatial evolution of Zagros collision zone in Kurdistan, NW Iran: constraints on Arabia–Eurasia oblique convergence. *Solid Earth, 7*, 659–672. https://doi.org/10.5194/se-7-659-2016

Talebian, M., & Jackson, J. (2004). A reappraisal of earthquake focal mechanisms and active shortening in the Zagros mountains of Iran. *Geophysical Journal International, 156*, 506–526. https://doi.org/10.1111/j.1365-246X.2004.02092.x

Tavani, S., Parente, M., Puzone, F., Corradetti, A., Gharabeigli, G., Valinejad, M., Morsalnejad, D., & Mazzoli, S. (2018). The seismogenic fault system of the 2017 Mw 7.3 Iran-Iraq earthquake: Constraints from surface and subsurface data, cross-section balancing, and restoration. *Solid Earth, 9*, 821–831. https://doi.org/10.5194/se-9-821-2018

Vajedian, S., Motagh, M., Mousavi, Z., Motaghi, K., Fielding, E. J., Akbari, B., Wetzel, H. U., & Darabi, A. (2018). Coseismic deformation field of the Mw 7.3 12 November 2017 Sarpol-e Zahab (Iran) earthquake: A decoupling horizon in the Northern Zagros Mountains inferred from InSAR observations. *Remote Sensing, 10*(1589). https://doi.org/10.3390/rs10101589

Vergés, J., Goodarzi, M. G. H., Emami, H., Karpuz, R., Efstathiou, J., & Gillespie, P. (2011). Multiple detachment folding in Pusht-e Kuh Arc, Zagros: Role of mechanical stratigraphy. *AAPG Memoir, 94*, 69–94. https://doi.org/10.1306/13251333M942899

Vernant, P., Nilforoushan, F., Hatzfeld, D., Abbassi, M. R., Vigny, C., Masson, F., Nankali, H., Martinod, J., Ashtiani, A., Bayer, R., Tavakoli, F., & Chéry, J. (2004). Present-day crustal deformation and plate kinematics in the Middle East constrained by GPS measurements in Iran and northern Oman. *Geophysical Journal International, 157*, 381–398. https://doi.org/10.1111/j.1365-246X.2004.02222.x

Walpersdorf, A., Hatzfeld, D., Nankali, H., Tavakoli, F., Nilforoushan, F., Tatar, M., Vernant, P., Chéry, J., & Masson, F. (2006). Difference in the GPS deformation pattern of North and Central Zagros (Iran). *Geophysical Journal International, 167*, 1077–1088. https://doi.org/10.1111/j.1365-246X.2006.03147.x

Wang, K., & Bürgmann, R. (2020). Probing fault frictional properties during afterslip updip and downdip of the 2017 Mw 7.3 Sarpol-e Zahab earthquake with space geodesy. *Journal of Geophysical Research: Solid Earth, 125*, e2020JB020319. https://doi.org/ 10.1029/2020JB020319

Wang, K., & Fialko, Y. (2014). Space geodetic observations and models of postseismic deformation due to the 2005 M7.6 Kashmir (Pakistan) earthquake. *Journal of Geophysical Research: Solid Earth, 119*, 7306–7318. https://doi.org/10.1002/2014JB011122

Wang, R., Lorenzo-Martín, F., & Roth, F. (2006). PSGRN/PSCMP - A new code for calculating co- and post-seismic deformation, geoid and gravity changes based on the viscoelastic-gravitational dislocation theory. *Computers and Geosciences, 32*, 527–541. https://doi.org/10.1016/j.cageo.2005.08.006

Wegmüller, U., Werner, C., Strozzi, T., Wiesmann, A., Frey, O., & Santoro, M. (2015). Sentinel-1A support in the GAMMA software, proc. of fringe 2015 workshop, Frascati, Italy, 23-27 march, ESA SP-731.

Wessel, P., & Smith, W. H. (1998). New, improved version of Generic Mapping Tools released. *Eos, Transactions American Geophysical Union, 79* (47), 579–579. https://doi.org/10.1029/98EO00426

Xu, G., Xu, C., Wen, Y., & Yin, Z. (2019). Coseismic and Postseismic Deformation of the 2016 Mw 6.2 Lampa Earthquake, Southern Peru, Constrained by Interferometric Synthetic Aperture Radar. *Journal of Geophysical Research: Solid Earth, 124*(4), 4250–4272. https://doi.org/10.1029/2018JB016572

Yang, Y. H., Hu, J. C., Yassaghi, A., Tsai, M. C., Zare, M., Chen, Q., Wang, Z. G., Rajabi, A. M., & Kamranzad, F. (2018). Midcrustal thrusting and vertical deformation partitioning constraint by 2017 Mw 7.3 Sarpol Zahab earthquake in Zagros Mountain Belt, Iran. *Seismological Research Letters, 89*(6), 2204–2213. https://doi.org/10.1785/0220180022

Yu, C., Li, Z., Penna, N. T., & Crippa, P. (2018). Generic atmospheric correction model for Interferometric Synthetic Aperture Radar observations. *Journal of Geophysical Research: Solid Earth, 123*(10), 9202-9222. https://doi.org/10.1029/2017JB015305

Referemces From Supporting Information

Feng, W., Li, Z., Hoey, T., Zhang, Y., Wang, R., Samsonov, S., et al. (2014). Patterns and mechanisms of coseismic and postseismic slips ofthe 2011 Mw7.1 Van (Turkey) earthquake revealed by multi-platform synthetic aperture radar interferometry. *Tectonophysics, 632*,188-198. https://doi.org/10.1016/j.tecto.2014.0 6.011

Feng, W., Lindsey, E., Barbot, S., Samsonov, S., Dai, K., Li, P., et al. (2017). Source characteristics of the 2015 MW7.8 Gorkha (Nepal)earthquake and its MW7.2 aftershock from space geodesy. *Tectonophysics, 712-713*, 747-758. https://doi.org/10.1016/j.tecto.2016.02.029